Spring 5-5-2011

Time-Resolved X-Ray Tomography of a Fluidized Bed of Geldart A Particles

Robert Frank Mudde
Delft University of Technology, r.f.mudde@tudelft.nl

Evert C. Wagner
Delft University of Technology, Netherlands

J.R. van Ommen
Delft University of Technology, Netherlands

Q. Ricoux
Delft University of Technology, Netherlands

TIME-RESOLVED X-RAY TOMOGRAPHY OF A FLUIDIZED BED OF GELDART A PARTICLES

R.F. Mudde[a], Q. Ricoux[b], E.C. Wagner[a] and J.R. van Ommen[b]
[a]Kramers Laboratorium voor Fysische Technologie (r.f.mudde@tudelft.nl)
[b]Department of Chemical Engineering
Delft University of Technology
Pr.Bernhardlaan 6, 2628 BW Delft, The Netherlands.

ABSTRACT
This paper discusses the influence of fines on the size of bubbles moving through a 23 cm ID fluidized bed of Geldart A particles imaged with an X-ray Tomographic Scanner. In earlier work [1], the bubble distribution in a fluidized bed of Geldart B particles was shown. The current study using Geldart A particles is more challenging to the reconstruction algorithm, since there are more bubbles, and they are smaller in size. We study the influence of adding fines (i.e. particles $\leq$ 45 micron) to the system. When adding a mass fraction of fines of 24%, we find a decrease of the average bubble of 40% of the size for the original powder, in line with earlier results from pressure probes and optical probes [2]. We find that the entire distribution of the bubble sizes shifts to smaller values.

INTRODUCTION

Many catalyzed gas reactions are performed in fluidized beds. The small particle size in combination with the low pressure drop are favorable for several applications. For higher gas through puts, part of the gas will flow through the fluidized bed in the form of void or bubbles. Although these bubbles are important when it comes to mixing of the powder, they have negative effects on the conversion as not all gas is now always in contact with the catalytic material. As shown in [2], a reduction of the bubble size by 40% may lead to an increase in conversion by 50%. Various papers have discussed the possibilities of reducing the bubble size. For instance, in [3] different gas injection strategies were employed. In the same article, the authors used electrical fields to influence the interparticle forces. In both cases a reduction of the bubble size was observed. The addition of fines is another possibility to improve the conversion [4], [5]. Beetstra et al. ([2]) reported experiments on the influence of fines on the fluidization behaviour of porous alumina particles. They added up to 50% fines to their powder and find, from pressure fluctuation analysis, a decrease of the average bubbles size with increasing mass fraction of fines. However, for the lower superficial gase velocities they investigated an increase was observed. Nevertheless, the trend was clear: for higher superficial gas velocities the average bubble size decreased monotonically with increasing mass fraction fines. From video images taken in a pseudo 2D bed, the authors found a clear shift in the bubble size distribution: for the higher gas velocities the entire distribution moved to smaller values with a smaller standard deviation (in absolute values).

In the present paper, we report experiments using our three source fast X-rays tomographic scanner and a 23cm fluidized bed. Tomographic systems have the advantage of being non-intrusive, while at the same time giving bubble properties such as size and shape. A few different tomographic techniques are in use, such as Electrical Capacitance Tomography (ECT, [6], [7]) and nuclear densitometry. ECT has the advantage of being fast and relatively cheap. However, its spatial resolution is problematic due to the soft nature of the electric fields used. The trajectory of the field lines is influenced by the gas-solid distribution, leading to a more cumbersome reconstruction ([8]). On the other hand, γ and X-rays are hard fields that, in prin-

ciple provide a better spatial resolution. They are, however, costly and due to inherent noise usually slow ([9], [10], [11], [12]). Recently, the time resolution of X-ray tomographic scanners has been considerably improved ([13], [14], [15], [16]).

We study the bubble size distribution of a Geldart A powder to which in steps a certain mass fraction of fines (particle size smaller than 45μm) is added. We reconstruct individual bubbles and measure their size. At the same time, we obtained the bubble frequency, by counting the number of bubbles passing the measuring plane in a given time interval.

EXPERIMENTAL SETUP

A 23cm inner-diameter perspex tube (wall thickness 5mm, height 71cm) is partially filled with powder. As the base case, the column is filled with alumina particles (mean particle size = 146 μm; particle density 1300 kg/m^3). These particles form a Geldart A powder close to the border of the A-B line. The minimum fluidization velocity is 0.008m/s. Additionally, different amounts of fines (also alumina) have been added during the experiments creating powders with a mass fraction of 0%, 8%, 16% and 24% of fines. The total amount of particles in the bed was kept at 14.5 kg, which gives a packed bed height of 40cm. The particle size distributions are given in table 1; the minimum fluidization velocity for each powder in table 2.

cumm. fraction (%)	10	25	50	75	90	mean
base material (μm)	104	121	143	169	195	146
fines (μm)	19.3	26.0	33.7	42.1	50.3	34.0

Table 1: Particle size distribution.

fraction fines (%)	0	8	16	24
U_{mf} (cm/s)	0.8	0.6	0.4	0.12

Table 2: Minimum fluidization velocity for the powders investigated.

Air (room temperature) is used as fluidization gas. It is either supplied via a wind box to the bed through a porous plate (sintered bronze, pore size 30 to 70μm, plate thickness 7mm), or via a single capillary (diameter 3.7mm) inserted in the bottom part of the bed. In the former case, the wind box is filled with 2mm glass beads to generate an as even as possible air flow into the bed. In the latter case the bed is not gassed through the porous plate: all air comes out of the capillary. On top of the bed an expanded section is placed (diameter 44cm, height 79cm) acting as a free board. The air leaving the set up first passed a filter before being vented to the surroundings. A schematic of the fluidized bed with the densitometer is given in Fig.1.

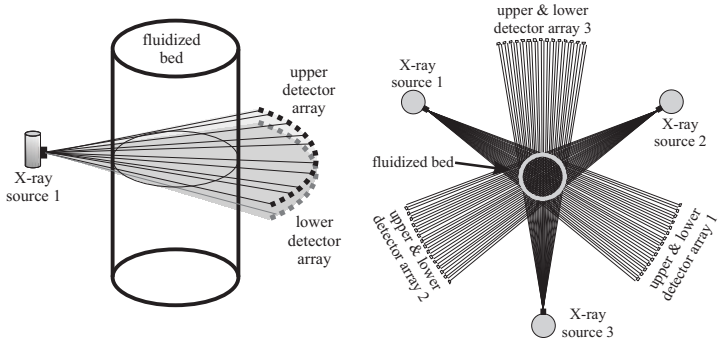

Figure 1: Schematic of the X-ray scanner. Left: side view showing for clarity only one source with its two detector arrays, right: top view.

The X-ray sources are placed at 120° around the fluidized bed. Each source generates a fan beam that is detected by two sets of 32 sensors placed opposite of the source. By using 2 sets, two measuring planes are formed located at 34.1cm and 36.0cm above the distributor plate, resp. The distance between the planes is 1.9cm. Comparing the raw signals allows estimation of the velocity of passing bubbles and from that the bubble size in the vertical direction. The distance from the X-ray-target to the center of the fluidized bed is 68.5cm, from the X-ray target to the detectors is 138.6cm. The fluidized bed is placed on a table that can be moved up and down in the vertical direction. This way we can adjust the height of the measuring plane in the column.

The X-ray sources used are manufactured by Yxlon International GmbH. The maximum X-ray energy is 150keV. We operate the sources at a low energy flux with a tube current less than 1mA. The detectors all consist of a $CdWO_4$ scintillation crystal optically coupled to a PIN photo diode. They are manufactured by Hamamatsu (type: S 1337 - 1010BR). Their crystal size is 10mm*10mm*10mm. A plastic casing in the form of an arc holds two horizontal arrays of 32 detectors. The curvature of the array is such that the distance to the focal point of the source is equal for all detectors. The data are collected simultaneously at a sampling frequency of 2500Hz, both for the upper and lower ring of detectors. The measured data are read out using a 12 bit ADC-card. The entire process is controlled via a workstation that sends out the trigger signals to the sources and reads out the detectors.

TOMOGRAPHIC RECONSTRUCTION

Measuring Principle

Each detector measures the attenuation of the X-rays in a thin cone. In the reconstruction this is treated as a thin line. If such a line of mono-energetic γ- or X-rays is transmitted through a closed system containing a particle-gas two-phase mixture, the number of photons registered per second, R, follows from the Lambert-Beer law:

$$R = R_0 exp\left[-\left((1-\alpha)\mu_p + \alpha\mu_g\right) d\right] \tag{1}$$

where R_0 is the number of photons registered per second when the system is in vacuum; μ_p and μ_g denote the linear absorption coefficient of the particle and gas phase; α is the volume fraction of the gas phase; d is the inner diameter of the system. It should be noted that the attenuation characteristics of the fluidized bed wall is incorporated in R_0. X-ray sources generate a wide spectrum of X-ray energies. The attenuation coefficients, μ_p and μ_g, are functions of the photon energy E. Therefore, a two-point calibration is inadequate, as the absorption of the photons of lower energy is much faster. In order to deal with this, we have calibrated all detector individually by placing various amounts of packed powder in between a source and its detectors. The amount of packed powder is put inside the column to ensure that the calibration encompasses the effects of the walls of the column. Furthermore, the calibration includes a completely empty and a completely filled bed. These two calibration points provide the upper and lower limit of the signal. We fitted a smooth function of the form $A_{cal} + B_{cal} \cdot exp\left(-x/C_{cal}\right)$ to the data, with x the distance traveled by the beam through the powder phase. For every detector, an individual curve is obtained, see [13].

Reconstruction

We use an Algebraic Reconstruction Technique. Although significantly slower than e.g. Linear Back Projection, algebraic methods offer more flexibility in terms of limited data sets and are more appropriate for the CT configuration system under consideration here. Detailed accounts of reconstruction techniques can be found in [17], [18] or [19].

We use the calibration curve to convert the measured line-averaged attenuation into a line averaged solids fraction. We will reconstruct the solids fraction $\alpha(x, y)$ in a pixel representation of the cross-section of the fluidized bed. Here, we use a square pixel array of 55*55 pixels. The cross-section of the fluidized bed exactly fits in this square. All pixels outside the circle have a

solids fraction of zero. For a given ray, traveling through the object, the total solids fraction on the line, p_i, referred to as *ray sum*, can be estimated as

$$\tilde{p}_i = \sum_{k=1}^{N} W_{ik}\alpha_k \tag{2}$$

with α_k the pixel-based value of the solids fraction distribution and W_{ik} the weighing factor for pixel k for the i^{th} ray through the object. We use a linear weighing matrix W. Hence, the weighing factor W_{ik} is the length of ray i through pixel k.

To reconstruct the image we need to solve the unknown pixel-averaged solids fraction α_k from eq.(2) for M different rays on N pixels. As the number of independent measurements is only 3*30=90 and the number of unknown pixels is easily 1000 or more, the problem is ill-posed. Moreover, there will be measuring noise in the data. The Algebraic Reconstruction Techniques (ART, see e.g. [17]) are designed to minimize the mismatch between the data $\vec{p}$ and $\mathbf{W} \cdot \vec{\alpha}$. They are iterative methods that solves $\vec{p} = \mathbf{W} \cdot \vec{\alpha}$. We use the Simultaneous Algebraic Reconstruction Technique (SART) [20]. Instead of sequentially updating the pixels on a ray-by-ray basis, SART simultaneously applies to a pixel the average of the corrections generated by all rays. This offers a reduction in the amplitude of the salt and pepper noise that is usually present in ART. However, it goes at the expense of the computation time. Still, pepper and salt noise will be present in the images. This can be reduced by using a so-called one-step-late algorithm (see [21]). We invoked an algorithm based on the median root function (suggested first by [22]). It effectively removes pepper and salt noise, but keeps the edges of larger objects sharp enough, see e.g. Mudde *et al.* [13] for full details about the reconstruction algorithm.

RESULTS AND DISCUSSION

X-ray sources are inherently noisy. This noise corrupts accurate reconstruction of the images of the bubbles as they are cut out by the measuring plane. Therefore, we have averaged the data first over a period of 10 data points and moved in steps of 10 time steps through the data series for each new reconstruction. This obviously reduces the time resolution of the images from 2500 frames per second to 250 frames per second. For the reconstructions a square pixel array of 55*55 pixels is used. The fluidized bed just fits in this square. Each pixel has a size of 4.188mm. Pixels outside the cross-sectional area of the fluidized bed are during the reconstruction set to zero. Fig.2 shows a quasi-3D reconstruction of the bubbling bed. The reconstructed images (at a frame rate of 250Hz) are stacked vertically. Note that the data are gathered in one plane: the vertical axis in the figure is time rather than the vertical coordinate (the two horizontal axis are in pixels; the unit for the vertical axis is 4ms). Note that the rectangular box shown in Fig.2 does not coincide with the outer dimensions of the fluidized bed, which is cylindrical in shape: a horizontal cross-section of the fluidized bed is a circle that exactly fits in a horizontal cut through Fig.2. Bubble travelling along the wall region of the fluidized bed, therefore look like moving internal through this box. However, they actually tough the wall of the bed.

It is noted here, that with the X-ray scanner and the reconstruction algorithm used we can confidently detect bubbles with a diameter of 2.5cm and above. Smaller bubbles can still be detected, but not with the same accuracy as the bigger ones. The influence of noise and small misalignments as well as the uncertainty in the calibration data put a lower limit to the diameter of the bubbles. To estimate the accuracy of small bubbles we performed a test on static phantoms. For this, we filled the bed with the Geldart A powder and places hollow cylinders of various diameters in the bed. In the measuring planes these cylinders should be visible as circular voids. As this is a steady state experiment there is no motion blurring and the measured data should yield the best possible reconstructions. For a cylinder with a diameter of 1.28cm, i.e. an area of 1.29cm^2, we reconstruct an area of 1.03cm^2, thus a diameter of only 1.14cm. if we put in more cylinders at the same time, reconstruction of the smaller ones

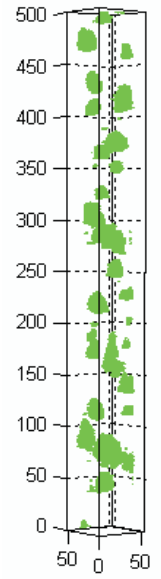

Figure 2: Reconstructed images stacked to form a quasi 3D image of the bubbles in the bed. The rectangular box does not show the wall of the fluidized bed, but is the stacking of the square reconstruction grid used.

becomes more problematic: occasionally ghost images of non-existing small cylinders show up. This is caused by noise in the data and by slight misalignment of the detectors. Note, that the value of each pixel is between 0 (fully packed) and 1 (no particles in pixel). To find the edge of teh bubbles, we used a threshold value of 0.5.

Gas Jet Experiments

Two types of experiments are performed. In the first one all air is sparged via a single capillary. This way a bubble train is generated. This has the advantage that we know a priori that only one bubble a time will be present in the reconstructed planes, making interpretation of the reconstructed solids distribution straight forward. The bubble diameter is obtained from the reconstructed images by taking the image in which a bubble shows its maximum area for each individual bubble. From that we estimate the bubble size according to $D_b = \frac{x_{max}-x_{min}+y_{max}-y_{min}}{2}$. Here, x_{max}, x_{min} denote the maximum, respectively minimum x-coordinate of all pixels comprising the bubble cross-sectional area, in the x-direction of the reconstruction grid. Similarly, y_{max}, y_{min} denote those in the y-direction. Subsequently, this bubble diameter is converted to centimeters using the known column diameter (23cm) and the number of grid points per direction (i.e. 55).

Experiments are run at two different gas velocities: U_{jet} = 46.5 cm/s and 93cm/s, i.e. a superficial velocity of 1.20cm/s and 2.41cm/s, resp. The averaged bubble size is computed from 10 different runs, each of 5 seconds data collecting and separated by 15 minutes between two subsequent runs. In total at least 140 bubbles are detected and used to compute the average bubble size. The effect of the mass fraction of fines is shown in Fig.3(a). It is clear from the data that the bubble size significantly decreases when increasing the mass fraction fines. From the measurements, we also obtain the bubble frequency, i.e. the number of bubbles passing the measuring plane per unit time, see Fig.3(b) where we show the bubble frequency for the high velocity jet case. The bubble frequency increases when increasing the mass fraction of fines. However, in the case of jet gassing, the increase of the frequency is only 30% for the lower gas velocity and 50% for the higher gas velocity case. Fig.3(a) shows a decrease of 40% of the mean bubble diameter. Consequently, based on the mean size, the bubble volume is only 22% of the bubble volume at 0% fines. Hence, the visible bubble rate, calculated as

$\phi_b = f_b V_b$, decreases to 28% of the visible bubble rate without the addition of fines for the lower gas inlet velocity and to 33% for the higher gas velocity used in the experiments. Apparently, considerably more gas is moving through the powder phase when introducing fines in the system. It should, however, be noted here that the bed is not fully fluidized; a considerably amount of the dense phase is in the packed state.

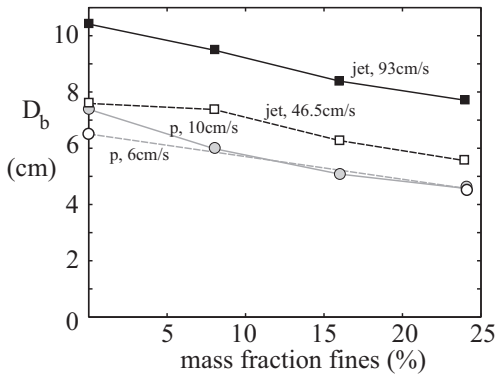

(a) Evolution of the bubble size as a function of the mass fraction fines: squares for the jet, black square U_{jet} = 93 cm/s, open square for U_{jet} = 46.5 cm/s; circles for the porous plate (denote by p), grey circle for U_{sup} = 10 cm/s, open circle for U_{sup} = 6 cm/s.

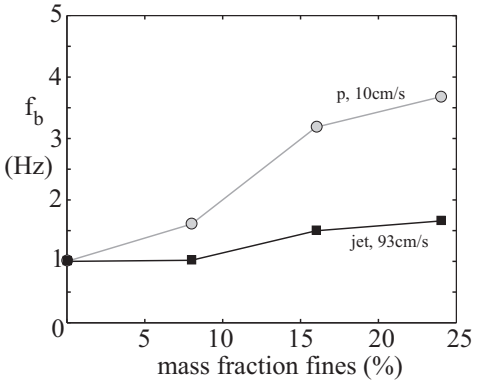

(b) Relative bubble size as a function of the mass fraction fines. Filled squares: jet U_{jet} = 93 cm/s, filled circles porous pate: U_{sup} = 10 cm/s.

Figure 3: Average bubble size and bubble frequency.

Fig.4 shows the bubble size distribution for U_{jet} = 46.5 cm/s for the original powder (0% fines) and for the 24% mass fraction fines case. Clearly the entire distribution has shifted to smaller values. Similar findings have been reported for a pseudo 2D bed, based on video images by [2]. For both cases shown in Fig.4 the standard deviation of the distribution is about 1.5 cm.

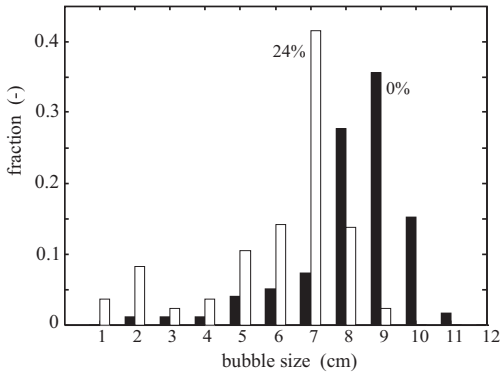

Figure 4: Bubble size distribution for two cases (U_{jet} = 46.5 cm/s): black bars 0% fines, white bars 24% fines.

Uniform Gassing

Similar experiments as described in the previous section have been performed using the porous plate as gas distributor. Although we tried to get the gas distribution as uniform as possible of the cross-section of the distributor of the plate, we observed that there was a slight tilt in the spatial bubble distribution. In Fig.3(a) also the average bubble size for gassing via the porous plate is shown as a function of the mass fraction fines for two superficial gas velocities, U_{sup} = 6.0 cm/s, 10.0 cm/s resp. Again, a clear decrease in bubble size is found. In this case the bubble size drops to only 60% of the original one. The values found are in reasonable

agreement with the Darton et al. equation [23], which predicts 5.7 and 4.5 cm diameter, respectively. However, the Darton et al. equation predict a slight increase in bubble diameter with increasing fines fraction (since the mimimum fluidization velocity is decreasing), while we find a strong decrease in bubble diameter. Fig.3(b) shows the increase in bubble frequency. For these conditions the increase in bubble frequency is much higher than for the jet-case. Consequently, the visible bubble rate drops less than in the jet experiments, but the drop is more relevant in this case, since the dense phase is fully fluidized at all fines fractions. At the highest mass fraction of fines (24%) the relative visible bubble rate is only 76% of that without fines. Clearly, a larger fraction of the gas flows through the particle phase when introducing fines. This is very important for catalyzed gas phase reactions, in which this will lead to higher conversions and often to higher selectivities.

CONCLUSIONS

In this paper, we used our fast X-ray tomographic scanner to investigate the influence on the bubble size when adding fines to a Geldart A powder (alumina, average particle size 146.4 μm; close to the B-border). We performed two experiments. In the first one, all gas is sparged through a single capillary, mounted in the bottom of the bed, into the powder. In the second one, the gas is introduced via a porous plate over the entire bottom of the fluidized bed. In both case the mass fraction of fines added was 8, 16 and 24%. We find a clear decrease in the bubble size and an increase in the bubble frequency. The average bubble size may decrease to only 60% of the mean bubble size without adding fines. The increase of the bubble frequency is insufficient to make up for this volume decrease and we conclude from the measurements that more gas flows through the powder mass when fines are present.

Our data agree with those reported by [2] based on pressure analysis and optical probes. The advantage of the X-ray scanner over pressure sensing is a more direct assessment of the bubble properties. Compared to the optical probe, the X-ray technique is, obviously, non-intrusive. Moreover, with the tomographic reconstruction the entire bubble is imaged, whereas the optical probe can only measure the chord length, which needs to be converted back, via a probabilistic approach, into the bubble size distribution. We can conclude that, due to its measuring speed, the X-ray tomographic scanner is a welcome new technique to experimentally study bubbling fluidized beds.

NOTATION

$A_{cal}, B_{cal}, C_{cal}$	calibration coefficient	
D_b	estimated bubble diameter	m
d	path length of beam through material	m
f_b	bubble frequency	$^{-1}$
p_i	total solids fraction on X-ray beam (ray sum)	-
R	photon count rate	s^{-1}
R_0	photon count rate in vacuum	s^{-1}
U_{jet}	gas velocity through capillary	m/s
U_{sup}	superficial gas velocity	m/s
V_b	bubble volume	m^3
v	velocity	m/s
W_{ik}	weighing matrix	-
x	path length of beam through powder phase	m
x, y	Cartesian coordinates in measuring plane	m
α	gas volume fraction	-
Δt	time interval	s
ϕ_b	visible bubble rate	m/s^3
μ_g	linear absorption coefficient of gas	m^{-1}
μ_p	linear absorption coefficient of particle	m^{-1}

REFERENCES

1. Mudde, R.F., Time-resolved X-ray tomography of a fluidized bed, *Powder Techn.*, 199, 55-59 (2010).
2. Beetstra, R., Nijenhuis, J., Ellis, N. and Van Ommen, J.R., The influence of the particle size distribution on fluidized bed hydrodynamics using high-throughput experimentation, *AIChE J.*, 55 (8), 2013-2023.
3. van Ommen, J.R., Nijenhuis, J., van den Bleek, C.M. and Coppens, M.O., Four ways to introduce structure in fluidized bed reactors, *Ind. & Eng. Chem. Res.*, 46, 4236-4244 (2007).
4. Yates, J.G. and Newton, D., Fine particle effects in a fluidized-bed reactor, *Chem. Eng. Sci.*, 41, 801-806 (1986).
5. Sun, G. and Grace, J.R., The effect of particle size distribution on the performance of a catalytic fluidized bed reactor, *Chem. Eng. Sci.*, 45, 2187-2194 (1990).
6. Beck, M. S., Dyakowski, T., and Williams, R. A., Process tomography - the state of the art, *Trans. Inst. Meas. and Control*, 20(4), 163-177 (1998).
7. Warsito, W. and Fan, L.-S., Dynamics of spiral bubble plume motion in the entrance region of bubble columns and three-phase fluidized beds using 3D ECT, *Chem. Eng. Sci.*, 60, 6073-6084 (2005).
8. Van Ommen, J.R. and Mudde, R.F., Measuring the Gas-Solids Distribution in Fluidized Beds - A Review, *Int. J. Chem. Reactor Eng.*, 6, Article no. R3 (2008).
9. Duduković, M.P., Opaque Multiphase Reactors: Experimentation, Modeling and Troubleshooting, *Oil & Gas Sci. Techn.*, 55 (2), 135-158 (2000).
10. Kumar, S.B., Moslemian, D. and Dudukovic, M.P., A γ-ray tomographic scanner for imaging voidage distribution in two-phase flow systems, *Flow Meas. Instr.*, 6 (1), 61-73 (1995).
11. Kumar, S.B., Moslemian, D. and Dudukovic, M.P., Gas holdup measurements in bubble columns using computed tomography, *AIChE J.*, 43, 1414-1425 (1997).
12. Mudde, R.F., Harteveld, W.K., Van den Akker, H.E.A., Van der Hagen, T.H.J.J. and Van Dam, H., Gamma radiation densitometry for studying the dynamics of fluidized beds, *Chem. Eng. Sci.*, 54, 2047-2054 (1999).
13. Mudde, R.F., Alles, J. and Van der Hagen, T.H.J.J., Feasibility study of a time-resolving X-ray tomographic system, *Meas. Sci. & Techn.*, 19, 085501 (2008).
14. Mudde, R.F., Bubbles in a fluidized bed: a fast X-ray scanner, *AIChE J.*, online: 29 Nov. (2010).
15. Bieberle, M. and Hampel, U., Evaluation of a limited angle scanned electron beam x-ray CT approach for two-phase pipe flows, *Meas. Sci. Technol.*, 17, 2057-2065 (2006).
16. Bieberle, M., Fischer, F., Schleicher, E., Hampel, U., Koch, D., Aktay, K.S.D.C., Menz, H.-J. and H.-G. Mayer, Ultrafast limited-angle-type x-ray tomography, *Appl. Phys. Lett., 91 (12)*, 123516 (2007).
17. Brooks, R. A. and DiChiro, G., Principles of computer assisted tomography (CAT) in radiographic and radioscopic imaging, *Phys. Med. Biol.*, 21, 689-732 (1976).
18. Herman, G. T., Image reconstruction from projections - the fundamentals of computerized tomography, Academic Press, 1980.
19. Kak, M. and Slaney, M., Principles of computerized tomographic imaging, IEEE Press, New York, 1988.
20. Andersen, A. H. and Kak, A. C., Simultaneous algebraic reconstruction technique (SART): a superior implementation of the ART algorithm, *Ultrasonic Imaging*, 6, 81-94 (1984).
21. Green, P. J., Bayesian reconstruction from emission tomography data using a modified EM algorithm, *IEEE Trans. on Med. Imag.*, 9, 84-93 (1990).
22. Alenius, S. and Ruotsalainen, U., Bayesian Image reconstruction for emission tomography based on median root prior, *Eur. J. of Nucl. Med.*, 24, 258-265 (1997).
23. Darton, R.C., La Nauze R.D., Davidson, J.F. and Harrison, D., Bubble growth due to coalescence in fluidised beds, *Trans. I. Chem. E.*, 55, 274-280 (1977).